Attribution of recent increases in atmospheric methane through 3-D inverse modelling

Joe McNorton[1,2], Chris Wilson[1,3], Manuel Gloor[4], Rob Parker[3,5], Hartmut Boesch[3,5], Wuhu Feng[1,6], Ryan Hossaini[7], Martyn Chipperfield[1,3]

[1.] School of Earth and Environment, University of Leeds, Leeds, UK.
[2.] Research Department, European Centre for Medium-Range Weather Forecasts, Reading, UK.
[3.] National Centre for Earth Observation, University of Leeds, Leeds, UK.
[4.] School of Geography, University of Leeds, Leeds, UK.
[5] Earth Observation Science Group, Department of Physics and Astronomy, University of Leicester, Leicester, UK.
[6]National Centre for Atmospheric Science, University of Leeds, Leeds, UK.
[7]Lancaster Environment Centre, Lancaster University, Lancaster UK.

Correspondence to: Joe McNorton (Joe.McNorton@ecmwf.int)

Abstract.

The atmospheric methane (CH_4) growth rate has varied considerably in recent decades. Unexplained renewed growth after 2006 followed seven years of stagnation and coincided with an isotopic trend toward CH_4 more depleted in ^{13}C, suggesting changes in sources and/or sinks. Using surface observations of both CH_4 and the isotopologue ratio value ($\delta^{13}CH_4$) to constrain a global 3D chemical transport model (CTM), we have performed a synthesis inversion for source and sink attribution. Our method extends on previous studies by providing monthly and regional attribution of emissions from 6 different sectors and changes in atmospheric sinks for the extended 2003-2015 period. Regional evaluation of the model CH_4 tracer with independent column observations from the Greenhouse gases Observing SATellite (GOSAT) shows improved performance when using posterior fluxes (R = 0.94-0.96, RMSE = 8.3-16.5 ppb), relative to prior fluxes (R = 0.60-0.92, RMSE = 48.6-64.6 ppb). Further independent validation with data from the Total Carbon Column Observing Network (TCCON) shows a similar improvement in the posterior fluxes (R = 0.90, RMSE = 21.4 ppb) compared to the prior (R = 0.71, RMSE = 55.3 ppb). Based on these improved posterior fluxes, the inversion results suggest the most likely cause of the renewed methane growth is a post-2006 1.8±0.4% decrease in mean OH, a 12.9±2.7% increase in energy sector emissions, mainly from Africa/Middle East and Southern Asia/Oceania, and a 2.6±1.8% increase in wetland emissions, mainly from Northern Eurasia. The posterior wetland increases are in general agreement with bottom-up estimates, but the energy sector growth is greater than estimated by bottom-up methods. The

model results are consistent across a range of sensitivity analyses performed. When forced to assume a constant (annually repeating) OH distribution, the inversion requires a greater increase in energy sector (13.6±2.7%) and wetland (3.6±1.8%) emissions but also introduces an 11.5±3.8% decrease in biomass burning emissions. Assuming no prior trend in sources and sinks slightly reduces the posterior growth

5 rate in energy sector and wetland emissions and further increases the amplitude of the negative OH trend. We find that possible tropospheric Cl variations do not to influence $\delta^{13}CH_4$ and CH_4 trends, although we suggest further work on Cl variability is required to fully diagnose this contribution. While the study provides quantitative insight into possible emissions variations which may explain the observed trends, uncertainty in prior source and sink estimates and a paucity of $\delta^{13}CH_4$ observations limit the accuracy of

10 the posterior estimates.

1 Introduction

The atmospheric concentration of methane (CH_4) has been increasing globally since 2007, following a slowdown in growth from 1999 to 2006 (Dlugokencky *et al.*, 2017). The onset of the observed increase in CH_4 coincides with an isotopic trend to lighter CH_4, more depleted in ^{13}C (Nisbet *et al.*, 2014). The $^{13}CH_4$:$^{12}CH_4$ ratio (denoted by the $\delta^{13}CH_4$ value) is controlled by

15 both the isotopic signatures of the sources and the isotopic fractionation associated with atmospheric CH_4 sinks. Broadly speaking, the emission types can be categorised into the relatively light biogenics (~-62‰), heavier fossil fuels (~-44‰) and the even heavier biomass burning emissions (~-22‰) (Schwietzke *et al.*, 2016). Isotopic fractionation in the atmosphere by the reaction with the hydroxyl (OH) radical and chlorine (Cl) atoms enriches $^{13}CH_4$, causing a background atmospheric $\delta^{13}CH_4$ of ~-47‰.

Previous studies have used simple global box-models for source and sink attribution of recent atmospheric CH_4 trends, with contradictory findings. Nisbet *et al*. (2014; 2016) and Schaefer *et al.* (2016) suggested that either increased wetland or agricultural emissions were the likely cause while Rigby *et al.* (2017) and Turner *et al.* (2017) found the most likely explanation to be a decreased global mean OH concentration, although they emphasised that the problem is not very well constrained by

25 existing data. These approaches are able to isolate the three emission categories noted above, and sometimes sink terms. Specific attribution, for example between wetlands and agricultural emission changes, requires spatial representation of both CH_4 and $\delta^{13}CH_4$. The box-model approach provides little or no information of spatial variation in posterior emission estimates, preventing regional attribution. Rice *et al*. (2016) performed a 3D chemical transport model (CTM) inversion using CH_4 and isotopologue measurements over the period 1984 to 2009. They found a 24 Tg yr^{-1} increase in fugitive fossil fuel emissions

30 between 1984 and 2009, most of which occurred after 2000. The trend in their inversion appeared similar to their prior emission

estimates. Although a 3D CTM is used in their study the posterior emissions are calculated globally and not regionally. Their study did not focus on the possible role of OH variations and did not consider inversions after 2009, so only captured two years of the continued post-2006 growth.

5   Here we perform a synthesis inversion using the TOMCAT 3-D CTM, building on previous work (Bousquet *et al.*, 2006; Bousquet *et al.*, 2011; Rigby *et al.*, 2012; Schwietzke *et al.*, 2016; Rice *et al.*, 2016) and using surface measurements of both CH_4 (Dlugokencky *et al.*, 2017) and $\delta^{13}CH_4$ (White *et al.*, 2017). We investigate regional source contributions and the roles of tropospheric OH and Cl in the recent growth of CH_4. From this we derive possible source and sink changes between 2003 and 2015 which best fit the observations.

10 2 Models and Observations

2.1 Chemical Transport Model

2.1.1 Forward model

The TOMCAT global CTM (Chipperfield *et al.*, 2006) has previously been widely used to simulate CH_4 trends and been evaluated against observations (e.g. Patra *et al.*, 2011; Wilson *et al.*, 2016; Parker *et al.*, 2018). Here we base CH_4 synthesis

15 inversions on TOMCAT simulations at $2.8° \times 2.8°$ resolution with 60 vertical levels from the surface to 60 km for 2003-2015. The simulations used meteorological forcing data from the 6-hourly European Centre for Medium-Range Weather Forecasts ERA-Interim reanalyses (Dee *et al.*, 2011). The model was spun up from a 1977 initialisation field before the mean global CH_4 and $\delta^{13}CH_4$ were rescaled to match NOAA observations in January 2002. A one-year inversion spin-up was then performed for 2002 and the results shown here begin in January 2003.

Methane emissions from McNorton *et al.* (2016a) were updated using revisions based on Schwietzke *et al.* (2016), which increased fossil fuel emissions and decreased biogenic emissions compared to the estimates in Kirschke *et al.* (2013). OH and stratospheric CH_4 loss fields were taken from McNorton *et al.* (2016b) and a TOMCAT-derived tropospheric Cl loss field (Hossaini *et al.*, 2016) was applied for the first time in our model.

Emissions were grouped into individual tracers for agriculture (excluding rice), biomass burning, energy, rice, waste, wetlands and 'supplementary', made up of the remaining sources (geological, hydrates, oceans and termites). Each source type, excluding 'supplementary', was then sub-divided into five geographic regions; North America (NA), Northern Eurasia (EA), South America (SA), Africa and Middle East (AM) and South Asia and Oceania (AO) (see Figure 6). To assess emission

30 variability over time, individual tracers were simulated for each month of the year, excluding 'supplementary' emissions, which were simulated annually. Emissions were further split into separate $^{12}CH_4$ and $^{13}CH_4$ tracers using isotopic source

signatures taken from Schwietzke *et al.*, (2016) (Table 1), resulting in 6 source types over 5 regions for 12 months and 2 isotopologues, with an additional 5 regions for 'supplementary' sources (a total of 730 tracers). Kinetic fractionation (KF, Table 1) was accounted for in the atmospheric loss of $^{13}CH_4$. The simulated tracers were then used to calculate CH_4 concentration and $\delta^{13}CH_4$ values. To investigate sensitivity to OH and Cl variations, three additional simulations were

5   performed, a control, an OH-enhanced simulation (1% increase) and a tropospheric Cl-enhanced simulation (1% increase).

2.1.2 Synthesis inversion

Our global synthesis inversions build on techniques used in Bousquet *et al.*, (2006), Bergamaschi *et al.*, (2007) and Rigby *et al.*, (2012). Prior estimates of sources and sinks, uncertainty estimates, and observations of both CH_4 and $\delta^{13}CH_4$ were used to quantify posterior estimates of sources and sinks. Posterior estimates were then used in a second forward simulation for the

10 same year, which provided an initialisation field for the subsequent year.

For the inversion including OH concentrations in the state vector we consider the total simulated CH_4 mixing ratio (φ) and the $\delta^{13}CH_4$ value (ψ) at time, t, at each measurement location, l. These are described as a linear combination of contributions from n_{reg} emission regions separated into n_{month} months and n_{source} emission sectors, loss due to OH, fractionation due to OH, the

15 initial mixing ratio at the location, φ_{ini}, and the initial $\delta^{13}CH_4$ value at the location, ψ_{ini}:

$$\varphi(\boldsymbol{x}, l, t) = \sum_{s=1}^{n_{source}} \sum_{i=1}^{n_{reg}} \sum_{m=1}^{n_{month}} x_{i,m,s} \frac{\Delta\chi}{\Delta x_{i,m,s}}(l,t) + x_{OH} \frac{\Delta\chi}{\Delta x_{OH}}(l,t) + x_{ini}\varphi_{ini}(l) \qquad (1)$$

$$\psi(\boldsymbol{x}, l, t) = \sum_{s=1}^{n_{source}} \sum_{i=1}^{n_{reg}} \sum_{m=1}^{n_{month}} x_{i,m,s} \frac{\Delta\psi}{\Delta x_{i,m,s}}(l,t) + x_{OH} \frac{\Delta\psi}{\Delta x_{OH}}(l,t) + \psi_{ini}(l) \qquad (2)$$

Note that we use Δ here to represent change, in order to avoid confusion with the isotopologue $\delta^{13}CH_4$. Basis functions $\frac{\Delta\chi}{\Delta x_{i,m,s}}$ and $\frac{\Delta\psi}{\Delta x_{i,m,s}}$ are sensitivities of atmospheric CH_4 and $\delta^{13}CH_4$ at a particular time and location to an emission of 1 Tg of CH_4 from a region i during a particular month m, for an emission sector s. Each $x_{i,m,s}$ is a scaling factor applied to the contribution from each basis function, and is initially set equal to the prior value of the emission. Similarly, $\frac{\Delta\chi}{\Delta x_{OH}}$ and $\frac{\Delta\psi}{\Delta x_{OH}}$ are the sensitivities of

25 the mixing ratio and $\delta^{13}CH_4$ at a measurement location to a change in the global OH concentration, linearised around the prior, and x_{OH} is initially set to be the prior OH concentration. x_{ini} is a dimensionless scaling factor initially set to be 1. Although the emissions in each region and source type are split into $^{12}CH_4$ and $^{13}CH_4$, the relative emissions of each isotopologue from each region for each source type are not included as separate basis functions. The 'state vector' $\boldsymbol{x}$ comprises of the individual

emission scaling factors $x_{i,m,s}$, for all i, m and s, along with x_{OH} and x_{ini}. Sensitivity experiments performed for tropospheric Cl follow the same formulation with Cl terms replacing OH terms.

Varying atmospheric CH_4 concentrations in the inversions results in a non-linear feedback on OH concentration. This feedback
5   is not accounted for and does not influence the offline OH field used in our inversion. To resolve this, an online OH field could in principle be used with an iterative minimization of the cost function; however, the variation in CH_4 concentration between the prior and posterior is relatively small and assumed to have a negligible influence on OH concentration.

The model OH is constrained by CH_4 and $\delta^{13}CH_4$ and not by other species, such as methyl-chloroform (MCF). MCF was
10   excluded because of uncertainty in emissions and a diminishing concentration (<5 ppt), particularly during the later period of the study (Liang *et al*., 2017). Due to the large uncertainty relative to the observed MCF concentrations in this period, including the extra species within the inversion would not add any extra constraint on the global OH concentration.

Independent inversions (INV-FULL) were performed for each year from 2003 to 2015. Initial conditions for each year are
15   provided by a forward simulation for the previous year driven by derived posterior emissions and loss rates, with 2003 initial conditions taken from a 2002 spin-up inversion. To estimate the flux contributions from each region we apply a minimisation function, which calculates the cost function, *J*:

$$J(\boldsymbol{x}) = \frac{1}{2}(\boldsymbol{x} - \boldsymbol{x}^b)^T.\boldsymbol{B}^{-1}.(\boldsymbol{x} - \boldsymbol{x}^b) + \frac{1}{2}(\boldsymbol{y} - \boldsymbol{G}.\boldsymbol{x})^T.\boldsymbol{R}^{-1}.(\boldsymbol{y} - \boldsymbol{G}.\boldsymbol{x}) \qquad (3)$$

The value of this 'cost function' is dependent on the value of the state vector $\boldsymbol{x}$. The vector $\boldsymbol{y}$ contains the observations. $\boldsymbol{x}^b$ is the *a priori* estimate of $\boldsymbol{x}$, and $\boldsymbol{B}$ is the error covariance matrix containing the uncertainties placed on the prior estimates, and the covariances between these uncertainties. $\boldsymbol{G}$ is the sensitivity matrix, which maps $\boldsymbol{x}$ onto the observations, and contains an array made up of the basis functions, $\frac{\Delta \chi}{\Delta x}$ and $\frac{\Delta \psi}{\Delta x}$ used in Eq. (1) and (2). $\boldsymbol{R}$ is the diagonal error covariance matrix for the
25   observations.

The minimum of the cost function is found using (Tarantola and Valette, 1982):

$$\boldsymbol{x}^a = \boldsymbol{x}^b + [\boldsymbol{G}^T.\boldsymbol{R}^{-1}.\boldsymbol{G} + \boldsymbol{B}^{-1}]^{-1}.\boldsymbol{G}^T.\boldsymbol{R}^{-1}.[\boldsymbol{y} - \boldsymbol{G}.\boldsymbol{x}^b] \qquad (4)$$

where $\boldsymbol{x}^a$ is the optimised set of scaling factors which minimise the value of *J*.

The posteriori error covariance matrix $\boldsymbol{A}$ is calculated from:

$$A = [G^T . R^{-1} . G + B^{-1}]^{-1} \qquad (5)$$

The initial prior uncertainty of each source within each region was set to 50%, based on uncertainties given by Kirschke *et al.*,
5   (2013). We assume that increased uncertainty in sources with large interannual variability is offset by those sources having
top-down (biomass burning) or process based (wetlands) interannually varying emissions in our simulations. We assumed
small variability in energy sector emissions so assigned a 1-month offset correlation of 0.5, we have not assigned correlations
between regions or months in the other prior emissions. Global annual OH and Cl are assumed to have an uncertainty of 2%;
for OH this is based on estimated interannual variability (Montzka *et al.*, 2011). The impact of varying these uncertainties was
10 investigated. Observational uncertainties were set at 10 ppb for CH_4 and 0.1‰ for $\delta^{13}CH_4$; the increase from the documented
uncertainties is to represent model transport uncertainty that would otherwise only be resolved by emission changes.

To investigate the effect of including $\delta^{13}CH_4$ observations we performed a separate inversion (INV-CH4) using only CH_4
observations. The difference between the inversions indicates the additional information supplied by the inclusion of $\delta^{13}CH_4$.
15 Additional sensitivity experiments were also performed, 9 with varying prior uncertainties and an additional one with no prior
trend in annual emissions, to investigate the robustness of the identified trends from the main inversion.

2.2 CH_4 and $\delta^{13}CH_4$ observations

Monthly mean measurements of CH_4 were taken from 21 National Oceanographic and Atmospheric Administration/Earth
System Research Laboratory (NOAA/ESRL) air sampling sites (Dlugokencky *et al.*, 2017) from 2003 to 2015, where available.
20 Measurements of $\delta^{13}CH_4$ were taken from 11 NOAA sampling sites and analysed by the Institute of Arctic and Alpine Research
(INSTAAR) (White *et al.*, 2017) for the same period (see Table 2). An equal weighting is applied to each monthly mean
measurement and potential cross correlations from neighbouring time steps and spatially nearby sites are not considered.

Column-averaged CH_4 (XCH_4) GOSAT satellite data provided by the University of Leicester were not included in the inversion
25 but retained for independent validation of the inversion results (Parker *et al.*, 2015). GOSAT was omitted because
measurements were only available from 2009, 6 years after the inversion began. The Total Carbon Column Observing Network
(TCCON) XCH_4 data were also used as validation but were considered too intermittent for use in the inversion (Wunch *et al.*,
2011).

3 Results

3.1 Synthesis Inversion

Inversion results constrained by CH_4 and $\delta^{13}CH_4$ observations (INV-FULL) show, as expected, improved seasonal and interannual monthly averaged posterior CH_4 and $\delta^{13}CH_4$ estimates when compared with assimilated surface observations

5 (Figure 1). The correlation with observations (R) for CH_4 increases from an all-site average of 0.72 in the prior to 0.94 in the posterior, and for $\delta^{13}CH_4$ increases from 0.52 to 0.87. Similarly, the root-mean-square error (RMSE) decreases from 38.2 ppb to 9.7 ppb for CH_4 and from 0.25‰ to 0.09‰ for $\delta^{13}CH_4$. The prior model captures some of the initial 2007 CH_4 growth but fails to capture the sustained growth (Figure 1a). The prior also shows a slight decrease in $\delta^{13}CH_4$ since 2007, but the magnitude of this is smaller than observed (Figure 1b). The renewed growth of CH_4 and corresponding decrease in $\delta^{13}CH_4$ in 2007 are

10 well captured in the inversion.

Inversion results constrained by CH_4 (INV-CH4), and not $\delta^{13}CH_4$, also accurately reproduce assimilated CH_4 observations (R = 0.93). INV-CH4 also shows some improved agreement with $\delta^{13}CH_4$ observations relative to the prior (R = 0.60), although values are overestimated in earlier years (2003-2008) (Figure 1b).

Validation of the model inversion using the independent, non-assimilated GOSAT data shows improved seasonal and interannual representation of XCH_4 (Figure 2). The RMSE is reduced in all 5 regions with values ranging from 48.6 to 64.6 ppb in the prior to 8.3 to 16.5 ppb in the posterior, with values typically originating from a negative bias in the model. The correlation is increased in the inversion with R values ranging from 0.60 to 0.92 in the prior to 0.94 to 0.96 in the posterior.

20 The trend is also better captured in the posterior in all 5 regions, although still underestimated in all regions, more so in EA (-1.3 ppb yr^{-1}) and AO (-1.1 ppb yr^{-1}). Both the prior and posterior biases are larger in the southern hemisphere, possibly as a result of slow inter-hemispheric transport within the model. Also contributing to this offset is an underestimation of southern hemisphere model growth in the prior model simulation (Figure 3).

25 Further validation is performed using measurements from 9 non-assimilated TCCON sites with data available from at least 2009 (see Table 3). The results show improved model correlation at all 9 sites, with an increase in the all-site mean R value from 0.71 in the prior to 0.90 in the posterior (Figure 4). Garmisch comparisons are the exception, where, for unknown reasons, neither the prior nor the posterior accurately captured the observed growth. The RMSE is reduced in in 8 out of 9 sites, with an all-site mean decrease from 55.3 ppb in the prior to 21.4 ppb in the posterior. Overall the inversions are found to noticeably

30 improve model performance when validated against the independent measurements from both GOSAT and TCCON. The resulting southern hemisphere offset in the posterior relative to GOSAT and TCCON suggests the posterior estimates represent a reasonable but not conclusive scenario for source/sink attribution. As only surface sites are assimilated, some inaccuracy in the representation of the total column is expected.

3.2 Source and Sink Attribution

The synthesis inversions, INV-FULL and INV-CH4, provide posterior regional changes in sources and global changes in OH (Figure 5). Relative to the prior, INV-FULL and INV-CH4 show an average OH decrease of 5% and 4%, respectively (Table 1). For the posterior time series, OH concentrations in INV-FULL and INV-CH4 are relatively constant throughout the period 2007-2015 (Figure 5) but these values are smaller by 1.8±0.4% and 0.3±0.5%, respectively, relative to their 2003-2006 concentrations. The larger drop post-2006 in INV-FULL OH concentration, relative to INV-CH4, highlights the importance of including $\delta^{13}CH_4$ in the inversion. The posterior OH error is reduced from the prior estimate of 2% to 1.8%, which, although a reduction, is similar to the modelled post-2007 OH decrease. The decrease in OH contributes to a decrease in $\delta^{13}CH_4$ and an increase in global CH_4.

Results from INV-FULL show that globally agricultural (-13%), energy (-8%) and biomass burning (+7%) emissions undergo the largest relative average 2003-2015 posterior change compared to the prior (Table 1). Relative changes in rice, waste and wetlands are smaller (<3%). The posterior emission errors are between 5%-13% compared with the 50% prior error. Average energy and wetland emissions are increased post-2007 by 12.9±2.7% (19.0 Tg yr^{-1}) and 2.6±1.8% (4.0 Tg yr^{-1}), respectively, relative to their 2003-2006 posterior values.

Regionally (Figure 6 and Table 4), 2003-2015 average posterior energy sector emissions are increased, relative to the prior, by 9-33% in four regions (NA, SA, AM and AO), which is offset by a 37% decrease in EA. Notable posterior agricultural emission decreases occur in EA (-36%) and AO (-14%). Wetland emissions are increased beyond the posterior error range in NA (+24%) and EA (+44%) and decreased within the error range in SA (-7%), AM (-7%) and AO (-6%). In all regions posterior emission estimates for biomass burning, waste and rice are within, or close to, the error range compared with prior estimates.

Our inversion results suggest that ~30% of the sustained CH_4 growth post-2006 can be explained by decreased OH, while ~60% and ~10% is attributed to increased energy sector and wetland emissions (Table 5). The shift in emissions between 2003-2006 and 2007-2015 is broadly consistent for each sector for three different inversions, INV_FULL, INV_CH4 and INV_FIXED (fixed annual emissions, see below) (Table 6). We investigated source and sink contribution to the negative $\delta^{13}CH_4$ trend using simple one box model analysis, outlined in the appendix of McNorton *et al.* (2016b), and posterior estimates from INV-FULL. Results show that post-2006 changes in energy sector (+0.15‰), biomass burning (-0.08‰), wetland (-0.05‰), waste sector (-0.03‰) and agricultural (-0.01‰) emissions, as well as OH (-0.12‰), contributed to the observed trend. Globally, for the 2003-2015 period, derived posterior and prior emission estimates had average growth rates of 4.1±0.6 Tg yr^{-2} and 4.0±0.2 Tg yr^{-2}, respectively. When considering only the renewed growth (2007-2015) the posterior growth rate of 5.7±0.8 Tg yr^{-2} becomes noticeably larger than the prior (3.7±0.4 Tg yr^{-2}). The post-2007 posterior growth occurs mainly in

the energy (3.4±1.0 Tg yr^{-2}) and wetland (1.4±1.0 Tg yr^{-2}) sectors. For the entire period most of the posterior energy sector growth occurred in AM (1.2 Tg yr^{-2}) and AO (1.5 Tg yr^{-2}), with a smaller proportion from NA (0.6 Tg yr^{-2}) and SA (0.2 Tg yr^{-2}) (Figure 6). Posterior wetland emission estimates show a growth of 0.8 Tg yr^{-2} for the 2003-2015 period, which increases to 1.4 Tg yr^{-2} for the 2007-2015 period. A majority of this growth occurs in EA (+0.5 Tg yr^{-2}). The four remaining emission

5   sectors all have a global annual change less than ±0.5 Tg yr^{-2}.

During the 2008-2012 period NA energy sector emissions were found to be 11.4 Tg yr^{-1} (+66%) higher than the 2003-2015 (excluding 2008-2012) average, resulting in uncertainty in the NA growth rate (Figure 5). These findings are also present in INV-CH4, which shows an 11.8 Tg yr^{-1} increase over the same period. This period of anomalously high emissions is not

10   present in the prior and therefore, is due to the assimilated observations.

The seasonal range of the prior global wetland emissions (5.7 Tg month^{-1}) is underestimated compared to the posterior (13.8 Tg month^{-1}). The seasonal cycle in biomass burning emissions is largely unchanged between the prior and posterior. The seasonal amplitude in rice emissions also remains largely unchanged, although the seasonal peak occurs in August in the prior

15   and July in the posterior.

Tropospheric Cl only accounts for a small fraction of the total CH$_4$ sink (~5%) (Kirschke *et al.*, 2013) but, as the KF influence of Cl is more than an order of magnitude greater than that of OH, it is plausible that changes in Cl contribute to the post-2007 trend in δ^{13}CH$_4$. Results from INV-CL (Figure 7) and the sensitivity setup with fixed OH (see Section 3.3) show similar

20   posterior fluxes. This suggests that Cl trends are unlikely to be an important contributor to the post-2007 CH$_4$ trends, although it is important to note that whilst variability was applied to prior emissions and the OH field, for some years, no variability is applied to the prior Cl field.

3.3 Sensitivity Tests

To test the robustness of the inversion to changes in prior error estimates we performed nine perturbation experiments (S1-

25   S9). Monthly source errors were perturbed between 10% and 100%, and yearly OH errors from 0% to 10% (Figure 8 and Table 7). For small error perturbations the inversion results do not change much relative to INV-FULL (Figure 8). However, when the emission errors are reduced from 50% to 10% (S4) the posterior energy emissions estimates deviate from the control (INV-FULL) inversion, with a mean bias of 60.5 Tg yr^{-1}. These large ranges in posterior estimates suggest the model fails to provide reasonable posterior estimates when the prior emission error is set too low. For most cases of increased emission errors the

30   OH change is similar to the control. However, for 100% emission errors (S6) the agricultural emissions are further reduced, from 82.8 Tg yr^{-1} in the prior and 72.1 Tg yr^{-1} in INV-FULL, to 64.1 Tg yr^{-1}. In this case OH is only reduced by 0.5% post-

2006, relative to 2003-2006, compared to 1.8% in INV-FULL. This results in a smaller OH contribution to the post-2006 CH_4 growth.

For a large or small OH errors (S3: 10%, S1: 1%) the posterior OH is decreased by 18% or 2%, respectively, compared to the prior OH. Assuming no change in OH (S9) post-2007 shifts in biomass burning, energy sector and wetland emissions relative to 2003-2006 are required to fit observations in the inversion. In this scenario biomass burning emissions decrease globally by -11.5±3.8% (-2.9 Tg yr^{-1}) and in AO by -16.1±17.9% (-1.2 Tg yr^{-1}). Energy sector emissions increase globally by 13.6±2.7% (+20.6 Tg yr^{-1}), in NA by 42.9±12.9% (+7.7 Tg yr^{-1}) and in AO by 36.7±5.1% (+12 Tg yr^{-1}). Wetland emissions increase globally by 3.6±1.8% (+5.8 Tg yr^{-1}). The sign and spatial distribution of these changes are similar to those seen in INV-FULL although the magnitude in post-2006 changes is typically increased in S9 (see Section 3.2).

The sensitivity simulations highlight that the prior uncertainty can have a noticeable influence on the posterior estimates. In particular, the posterior OH is found to be sensitive to the prior error estimate, highlighting the importance of prior knowledge for future studies. This limits the accuracy of the magnitude of the posterior estimates. However, the spatial, temporal and sector specific relative post-2007 changes, compared to 2003-2006, remain broadly consistent between experiments.

We performed a synthesis inversion with no prior trend in emissions or OH (INV-FIXED), using fixed 2003 emissions, to investigate the sensitivity of the inversion to prescribed prior trend information (Figure 9). The results show an annual average CH_4 emission growth of 2.8±0.6 Tg yr^{-2}, a majority of which comes from the energy sector (1.8±0.6 Tg yr^{-2}) and wetlands (0.7±0.5 Tg yr^{-2}). On a global scale the sector attribution agrees well with INV-FULL but with a smaller magnitude in emission trends. The reduced growth in INV-FIXED is offset by a higher negative trend in OH concentration (-0.23% yr^{-1}), relative to INV_FULL (-0.14% yr^{-1}).

In absolute terms OH concentrations are 0.8% lower in INV-FIXED compared to INV-FULL, which acts to offset the lower emissions. OH concentrations for INV-FIXED are 1.8% lower for the 2007-2015 period, relative to the 2003-2006 period, matching the relative change from INV-FULL. Regionally, the largest trends are observed over NA (1.2±0.9 Tg yr^{-2}), AM (0.9±0.3 Tg yr^{-2}) and AO (0.7±0.4 Tg yr^{-2}), with over half of the growth in each of those regions originating from the energy sector. Overall INV-FIXED shows good spatial agreement with INV-FULL when considering sector attribution but the magnitude of emission increases is slightly smaller.

4 Conclusions

We have performed a synthesis inversion using a 3D CTM to investigate the post-2007 renewed growth in atmospheric CH_4 and decline in $\delta^{13}CH_4$. This work extends on previous work, which was based on a box-model approach for source and sink

attribution based on CH_4 and $\delta^{13}CH_4$ observations (e.g. Rigby *et al.*, 2017). By using a 3D CTM we have been able to provide detailed monthly regional attribution of 6 different emission sectors and global OH changes, evaluating both the trends over the full 2003-2015 period and shifts that occurred around 2007. We have also been able to validate these results using recent XCH_4 data available from GOSAT and TCCON. The sensitivity of the inversion has been tested for different prior assumptions

5   and uncertainties.

A CH_4-only inversion underconstrains the solution with respect to $^{13}CH_4$ observations, resulting in larger errors. The constraint improves when the $\delta^{13}CH_4$ observations are introduced. The prior model based on published emissions does not capture the CH_4 and $\delta^{13}CH_4$ trend in both the assimilated surface site observations and the non-assimilated GOSAT and TCCON data. In

10   contrast, our derived posterior emission inventories capture both the renewed growth in CH_4 and the reduction in $\delta^{13}CH_4$ observed from the assimilated NOAA surface sites from 2007-2015, and compare well with independent GOSAT and TCCON-derived XCH_4. The independent validation suggests that, although the CH_4 growth rate is better represented in the posterior, it is still underestimated. The magnitude of the contribution of model transport error to this underestimation is unknown. Both prior and posterior simulations underestimate southern hemisphere CH_4 concentrations, highlighting possible issues with

15   interhemispheric transport within the model. The lack of independent data around the end of the CH_4 'hiatus' means it is difficult to evaluate model performance over this period (2007).

Our inversion results suggest that the 2007-2015 growth in CH_4 can be best explained by a 1.8±0.4% reduction in mean OH, a 12.9±2.7% increase in energy sector emissions, mainly from AM and AO, and a 2.6±1.8% increase in wetland emissions,

20   mainly from EA. The recent EDGAR v4.3.2 inventory (Janssens-Maenhout *et al.,* 2017) for energy sector emissions shows AM and AO growth of 1.0 Tg yr^{-2} and 2.4 Tg yr^{-2}, respectively, for 2003-2012. These are, however, smaller than the 2.2 Tg yr^{-2} and 3.1 Tg yr^{-2} shown by our inversion for the same period. A majority of prior AM energy sector emissions originate from energy for buildings in Nigeria and Eastern Africa, fuel exploitation from The Middle East, The Niger Delta and South Africa, and pipelines in Western Africa, Algeria and The Middle East. As a result emissions from these regions are influenced

25   by posterior emission changes and assumed to be underestimated in both magnitude and growth rate in the prior. For the AO energy sector, a majority of prior emissions, and therefore the posterior increases, originate from energy for buildings in India, China and South-East Asia, fuel exploitation in Eastern China, Japan, India, South East Asia and Eastern Australia, refineries in Northern India, Eastern China, Japan and Indonesia, and pipelines in India Eastern China, Eastern Australia and New Zealand. The growth in emissions in EA in EDGAR v4.3.2 (1.4 Tg yr^{-2}) is not seen in our inversion for the same region and

30   period (-2.2 Tg yr^{-2}). We also find higher-than-average (2005-2015) energy sector emissions over NA between 2008 and 2012, which may be associated with oil or natural gas extraction (Helmig *et al.*, 2016). The expected increase in atmospheric $\delta^{13}CH_4$ caused by increased energy sector emissions (+0.15‰) is offset mainly by the decrease in OH (-0.12‰), small decrease in biomass burning emissions (-0.08‰) and small increase in wetland emissions (-0.05‰).

The small increase in wetland emissions since 2007 derived from the inversion agrees well bottom-up estimates for wetland emission trends, for example the 3% increase found by McNorton *et al*. (2016a). A decrease in OH as a contributor to the renewed growth agrees well with previous simple global box models (Rigby *et al.,* 2017; Turner *et al.*, 2017). The OH shift found here is smaller in magnitude than the -8% shift between 2004 and 2014 derived by Rigby *et al.*, (2017) using AGAGE measurements. Our results show a small negative shift in posterior biomass burning emissions (-2.9 Tg yr^{-1}) for 2007-2015 period relative to 2003-2006, in agreement with the 3.7 Tg CH_4 yr^{-1} decrease derived by Worden *et al.* (2017) for the 2008-2014 period relative to 2001-2007.

When $\delta^{13}CH_4$ is not assimilated the trend in posterior emissions is slightly increased post-2006 and the OH decrease is smaller (-0.3%). By including the $\delta^{13}CH_4$ observations a larger post-2006 OH decrease is required (-1.8%), highlighting the importance of including $\delta^{13}CH_4$ within the inversion.

An alternative scenario, where OH is assumed constant post-2007, requires a -11.5±3.8% decrease in biomass burning emissions, and 13.6±2.7% and 3.6±1.8% increases in energy sector and wetland emissions. These results agree with previous studies, which also assumed constant OH (Nisbet *et al*., 2016; Schaefer *et al.*, 2016; Worden *et al*., 2017). If no change in OH has occurred then this presents an alternative explanation for the cause of the post-2007 CH_4 growth.

The inversion results suggest Eurasian energy sector emissions are typically overestimated by inventories, such as the Global Carbon Budget (Saunois *et al*., 2016). The reduced EA emissions are found to be offset by an underestimate in all other regions. We find prior annual estimates of biomass burning, waste and rice to be relatively accurate, whilst agricultural estimates are overestimated. Small changes occur in the seasonal cycle of rice emissions and the seasonal range is underestimated in wetland emissions.

The inversion is found to be robust when small changes are made to uncertainty errors; however, large uncertainty remains around the accuracy of prior emissions. Assuming no prior trend in emissions reduces the required growth rate in both wetland and energy sector emissions, although they remain the main source contribution to the renewed growth post-2006. The reduction in the emission trend is offset by an increased negative trend in OH concentration. Overall the magnitude of the trends inferred varies between experiments but there is consistent agreement that both OH decrease and, wetland and energy sector emission increase contributed to the post-2006 growth.

Our inversion results represent plausible scenarios for variations in CH_4 sources and sinks, though several caveats exist. The uncertainties in the sources and sinks are somewhat subjective and we have not considered source signature and KF uncertainty. We have assumed that all uncertainties are independent of each other (excluding energy emissions). We have also not considered variation in other sinks (e.g. $O(^1D)$, soil). Finally, an important question is whether tropospheric OH has varied in

the way suggested by CH$_4$ inversions studies. The processes causing variations in OH are complex and remain poorly quantified. Possible explanations include changes in tropospheric O$_3$ and trends in tropospheric UV radiation related to global stratospheric O$_3$ recovery. If the reduction in available OH due to increased reactive carbon gases is no longer being sufficiently offset by increased emissions of OH-forming nitrogen oxides, then OH concentrations might be in decline (Lelieveld *et al.*,

5   2004).

Acknowledgments, Samples, and Data

This work was supported by the NERC MOYA project (NE/N015657/1). MPC and MG acknowledge support from NERC grants GAUGE (NE/K002244/1) and AMAZONICA (NE/F005806/1). RJP was funded via an ESA Living Planet Fellowship with additional funding from the UK National Centre for Earth Observation and the ESA Greenhouse Gas Climate Change

10   Initiative (GHG-CCI). HB was supported by ESA GHG-CCI. CW, RJP and HB acknowledge funding support as part of NERC's National Centre for Earth Observation, contract number PR140015. The TOMCAT runs were performed on the Arc3 supercomputer at U. Leeds. We thank the Japanese Aerospace Exploration Agency, National Institute for Environmental Studies, and the Ministry of Environment for the GOSAT data and their continuous support as part of the Joint Research Agreement. The GOSAT retrievals used the ALICE High Performance Computing Facility at the University of Leicester.

15   NOAA atmospheric CH$_4$ and δ^{13}CH$_4$ values were obtained from the ESRL GMD Carbon Cycle Cooperative Global Air Sampling Network (esrl.noaa.gov). TCCON atmospheric column CH$_4$ values were obtained from the TCCON data achieve (tccondata.org). The authors would also like to thank Matt Rigby for advice with ^{13}CH$_4$ modelling.

All model data used in this study are available through the University of Leeds ftp server. For access please contact

20   M.Chipperfield@leeds.ac.uk.

References

Bergamaschi, P., Frankenberg, C., Meirink, J.F., Krol, M., Dentener, F., Wagner, T., Platt, U., Kaplan, J.O., Körner, S., Heimann, M. and Dlugokencky, E.J.: Satellite chartography of atmospheric methane from SCIAMACHY on board ENVISAT: 2. Evaluation based on inverse model simulations, *J. Geophys. Res.: Atmos.*, *112*, D02304, doi: 10.1029/2006JD007268, 2007.

Blumenstock, T., Hase, F., Schneider, M., Garc*í*a, O.E. and Sepúlveda, E.: TCCON data from Izana, Tenerife, Spain, Release GGG2014R1. TCCON data archive, hosted by CaltechDATA, California Institute of Technology, Pasadena, CA, U.S.A., doi:10.14291/tccon.ggg2014.izana01.R1, 2017.

Bousquet, P., Ciais, P., Miller, J.B., Dlugokencky, E.J., Hauglustaine, D.A., Prigent, C., Van der Werf, G.R., Peylin, P., Brunke, E.G., Carouge, C. and Langenfelds, R.L.: Contribution of anthropogenic and natural sources to atmospheric methane variability, *Nature*, *443*, 439-443, doi:10.1038/nature05132, 2006.

5   Bousquet, P., Ringeval, B., Pison, I., Dlugokencky, E.J., Brunke, E.G., Carouge, C., Chevallier, F., Fortems-Cheiney, A., Frankenberg, C., Hauglustaine, D.A. and Krummel, P.B.: Source attribution of the changes in atmospheric methane for 2006–2008, *Atmos. Chem. Phys.*, *11*, 3689-3700, doi:10.5194/acp-11-3689-2011, 2011.

Chipperfield, M.: New version of the TOMCAT/SLIMCAT off-line chemical transport model: Intercomparison of stratospheric tracer experiments, *Q. J. Roy. Meteorol. Soc.*, *132*, 1179-1203, doi:10.1256/qj.05.51, 2006.

Dee, D.P., Uppala, S.M., Simmons, A.J., Berrisford, P., Poli, P., Kobayashi, S., Andrae, U., Balmaseda, M.A., Balsamo, G., Bauer, D.P. and Bechtold, P.: The ERA-Interim reanalysis: Configuration and performance of the data assimilation system, *Q. J. Roy. Meteorol. Soc.*, *137*, 553-597, doi:10.1002/qj.828, 2011.

15   Dlugokencky, E.J., Lang, P.M., Crotwell, A.M., Mund, J.W., Crotwell, M.J. and Thoning, K.W.: Atmospheric Methane Dry Air Mole Fractions from the NOAA ESRL Carbon Cycle Cooperative Global Air Sampling Network, 1983-2016, Version: 2017-07-28, Path: ftp://aftp.cmdl.noaa.gov/data/trace_gases/ch4/flask/surface/, 2017.

Griffith, D. W. T., *et al*.: TCCON data from Darwin, Australia, Release GGG2014R0. TCCON data archive, hosted by
20   CaltechDATA, California Institute of Technology, Pasadena, CA, U.S.A. doi:10.14291/tccon.ggg2014.darwin01.R0/1149290, 2017a.

Griffith, D. W. T., Velazco, V. A., Deutscher, N., Murphy, C., Jones, N., Wilson, S., Macatangay, R., Kettlewell, G., Buchholz, R. R., Riggenbach, M.: TCCON data from Wollongong, Australia, Release GGG2014R0. TCCON data archive, hosted by
25   CaltechDATA, California Institute of Technology, Pasadena, CA, U.S.A. doi:10.14291/tccon.ggg2014.wollongong01.R0/1149291, 2017b.

Helmig, D., Rossabi, S., Hueber, J., Tans, P., Montzka, S.A., Masarie, K., Thoning, K., Plass-Duelmer, C., Claude, A., Carpenter, L.J. and Lewis, A.C.: Reversal of global atmospheric ethane and propane trends largely due to US oil and natural
30   gas production, *Nat. Geosci.*, *9*, 490-495, doi:10.1038/ngeo2721, 2016.

Hossaini, R., Chipperfield, M.P., Saiz-Lopez, A., Fernandez, R., Monks, S., Feng, W., Brauer, P. and Glasow, R.: A global model of tropospheric chlorine chemistry: Organic versus inorganic sources and impact on methane oxidation, *J. Geophys. Res.*, *121*, 14271-14297, doi:10.1002/2016JD025756, 2016.

Janssens-Maenhout, G., Crippa, M., Guizzardi, D., Muntean, M., Schaaf, E., Dentener, F., Bergamaschi, P., Pagliari, V., Olivier, J.G.J., Peters, J.A.H.W. and Van Aardenne, J.A.: EDGAR v4.3.2 Global Atlas of the three major Greenhouse Gas Emissions for the period 1970-2012, *Earth Sys. Sci. Data Discuss.,* in review, doi:10.5194/essd-2017-79, 2017.

Kirschke, S., Bousquet, P., Ciais, P., Saunois, M., Canadell, J.G., Dlugokencky, E.J., Bergamaschi, P., Bergmann, D., Blake, D.R., Bruhwiler, L. and Cameron-Smith, P.: Three decades of global methane sources and sinks, *Nat. Geosci.*, *6*, 813-823, doi:10.1038/ngeo1955, 2013.

10   Kivi, R., Heikkinen, P. and Kyro, E.: TCCON data from Sodankyla, Finland, Release GGG2014R0. TCCON data archive, hosted by CaltechDATA, California Institute of Technology, Pasadena, CA, U.S.A. doi:10.14291/tccon.ggg2014.sodankyla01.R0/1149280, 2017.

Lelieveld, J., Dentener, F.J., Peters, W. and Krol, M.C.: On the role of hydroxyl radicals in the self-cleansing capacity of the
15   troposphere, *Atmos. Chem. Phys.*, *4*, 2337-2344, doi:10.5194/acp-4-2337-2004, 2004.

Liang, Q., Chipperfield, M.P., Fleming, E.L., Abraham, N.L., Braesicke, P., Burkholder, J.B., Daniel, J.S., Dhomse, S., Fraser, P.J., Hardiman, S.C. and Jackman, C.H.: Deriving Global OH Abundance and Atmospheric Lifetimes for Long-Lived Gases: A Search for CH3CCl3 Alternatives, *J. Geophys. Res.: Atmos.*, *122*, 11914-11933, doi:10.1002/2017JD026926, 2017.

McNorton, J., Gloor, E., Wilson, C., Hayman, G.D., Gedney, N., Comyn-Platt, E., Marthews, T., Parker, R.J., Boesch, H. and Chipperfield, M.P.: Role of regional wetland emissions in atmospheric methane variability. *Geophys. Res. Lett.*, *43(21)*, L11433, doi:10.1002/2016GL070649, 2016.

25   McNorton, J., Chipperfield, M.P., Gloor, M., Wilson, C., Feng, W., Hayman, G.D., Rigby, M., Krummel, P.B., O'Doherty, S., Prinn, R.G. and Weiss, R.F.: Role of OH variability in the stalling of the global atmospheric CH_4 growth rate from 1999 to 2006, *Atmos. Chem. Phys.*, *16*, 7943-7956, doi:10.5194/acp-16-7943-2016, 2016.

Montzka, S.A., Krol, M., Dlugokencky, E., Hall, B., Jöckel, P. and Lelieveld, J.: Small interannual variability of global
30   atmospheric hydroxyl, *Science*, *331*, 67-69, doi:10.1126/science.1197640, 2011.

Nisbet, E.G., Dlugokencky, E.J. and Bousquet, P.: Methane on the rise—again, *Science*, *343(6170)*, 493-495, doi:10.1126/science.1247828, 2014.

Nisbet, E.G., Dlugokencky, E.J., Manning, M.R., Lowry, D., Fisher, R.E., France, J.L., Michel, S.E., Miller, J.B., White, J.W.C., Vaughn, B. and Bousquet, P.: Rising atmospheric methane: 2007–2014 growth and isotopic shift, *Global Biogeochem. Cycles*, *30(9)*, 1356-1370, doi:10.1002/2016GB005406, 2016.

5   Notholt, J., Schrems, O., Warneke, T., Deutscher, N., Weinzierl, C., Palm, M., Buschmann, M., and AWI-PEV Station Engineers: TCCON data from Ny Alesund, Spitzbergen, Norway, Release GGG2014R0. TCCON data archive, hosted by CaltechDATA, California Institute of Technology, Pasadena, CA, U.S.A. doi:10.14291/tccon.ggg2014.nyalesund01.R0/1149278, 2017a.

10 Notholt, J., Petri, C., Warneke, T., Deutscher, N., Buschmann, M., Weinzierl, C., Macatangay, R. and Grupe, P.: TCCON data from Bremen, Germany, Release GGG2014R0. TCCON data archive, hosted by CaltechDATA, California Institute of Technology, Pasadena, CA, U.S.A. doi:10.14291/tccon.ggg2014.bremen01.R0/1149275, 2017b.

Parker, R., Boesch, H., Byckling, K., Webb, A.J., Palmer, P.I., Feng, L., Bergamaschi, P., Chevallier, F., Notholt, J. and
15 Deutscher N.: Assessing 5 years of GOSAT Proxy XCH_4 data and associated uncertainties, *Atmos. Meas. Tech.*, *8*, 4785-4801, doi:10.5194/amtd-8-5937-2015, 2015.

Patra, P.K., Houweling, S., Krol, M., Bousquet, P., Belikov, D., Bergmann, D., Bian, H., Cameron-Smith, P., Chipperfield, M.P., Corbin, K. and Fortems-Cheiney, A.: TransCom model simulations of CH_4 and related species: linking transport, surface
20 flux and chemical loss with CH_4 variability in the troposphere and lower stratosphere, *Atmos. Chem. Phys.*, *11*, 12813-12837, doi:10.5194/acp-11-12813-2011, 2011.

Rice, A.L., Butenhoff, C.L., Teama, D.G., Röger, F.H., Khalil, M.A.K. and Rasmussen, R.A.: Atmospheric methane isotopic record favors fossil sources flat in 1980s and 1990s with recent increase, *Proc. Natl. Acad. Sci.*, *113(39)*, 10791-10796,
25 doi:10.1073/pnas.1522923113, 2016.

Rigby, M., Manning, A.J. and Prinn, R.G.: The value of high-frequency, high-precision methane isotopologue measurements for source and sink estimation, *J. Geophys. Res.*, *117*, D12312, doi:10.1029/2011JD017384, 2012.

30 Rigby, M., Montzka, S.A., Prinn, R.G., White, J.W., Young, D., O'Doherty, S., Lunt, M.F., Ganesan, A.L., Manning, A.J., Simmonds, P.G. and Salameh, P.K.: Role of atmospheric oxidation in recent methane growth, *Proc. Natl. Acad. Sci.*, *114(21)*, 5373-5377, doi:10.1073/pnas.1616426114, 2017.

Saunois, M., et al.: The global methane budget 2000–2012, *Earth Syst. Sci. Data*, *8*, 697-751, doi: 10.5194/essd-8-697-2016, 2016.

Schaefer, H., Fletcher, S.E.M., Veidt, C., Lassey, K.R., Brailsford, G.W., Bromley, T.M., Dlugokencky, E.J., Michel, S.E., Miller, J.B., Levin, I. and Lowe, D.C.: A 21st-century shift from fossil-fuel to biogenic methane emissions indicated by $^{13}CH_4$, *Science*, *352*, 80-84, doi:10.1126/science.aad2705, 2016.

Schwietzke, S., Sherwood, O.A., Bruhwiler, L.M., Miller, J.B., Etiope, G., Dlugokencky, E.J., Michel, S.E., Arling, V.A., Vaughn, B.H., White, J.W. and Tans, P.P.: Upward revision of global fossil fuel methane emissions based on isotope database, *Nature*, *538(7623)*, 88-91, doi:10.1038/nature19797, 2016.

Sussmann, R. and Rettinger, M.: TCCON data from Garmisch, Germany, Release GGG2014R1. TCCON data archive, hosted by CaltechDATA, California Institute of Technology, Pasadena, CA, U.S.A. https://doi.org/10.14291/tccon.ggg2014.garmisch01.R1, 2017.

Turner, A.J., Frankenberg, C., Wennberg, P.O. and Jacob, D.J.: Ambiguity in the causes for decadal trends in atmospheric methane and hydroxyl, *Proc. Natl. Acad. Sci.*, *114(21)*, 5367-5372, doi:10.1073/pnas.1616020114, 2017.

Wennberg, P. O., Roehl, C., Wunch, D., Toon, G. C., Blavier, J.-F., Washenfelder, R., Keppel-Aleks, G., Allen, N. and Ayers, J.: TCCON data from Park Falls, Wisconsin, USA, Release GGG2014R1. TCCON data archive, hosted by CaltechDATA, California Institute of Technology, Pasadena, CA, U.S.A. doi:10.14291/tccon.ggg2014.parkfalls01.R1, 2017a.

Wennberg, P. O., Wunch, D., Roehl, C., Blavier, J.-F., Toon, G. C., Allen, N., Dowell, P., Teske, K., Martin, C. and Martin, J.: TCCON data from Lamont, Oklahoma, USA, Release GGG2014R1. TCCON data archive, hosted by CaltechDATA, California Institute of Technology, Pasadena, CA, U.S.A. doi:10.14291/tccon.ggg2014.lamont01.R1/1255070, 2017b.

White, J.W.C., Vaughn, B.H. and Michel, S.E.: University of Colorado, Institute of Arctic and Alpine Research (INSTAAR), Stable Isotopic Composition of Atmospheric Methane (13C) from the NOAA ESRL Carbon Cycle Cooperative Global Air Sampling Network, 1998-2015, Version: 2017-01-20, Path: ftp://aftp.cmdl.noaa.gov/data/trace_gases/ch4c13/flask/, 2017.

Worden, J.R., Bloom, A.A., Pandey, S., Jiang, Z., Worden, H.M., Walker, T.W., Houweling, S. and Röckmann, T.: Reduced biomass burning emissions reconcile conflicting estimates of the post-2006 atmospheric methane budget, *Nat. Commun.*, *8(1)*, 2227, doi:10.1038/s41467-017-02246-0, 2017.

Wilson, C., Gloor, M., Gatti, L.V., Miller, J.B., Monks, S.A., McNorton, J., Bloom, A.A., Basso, L.S. and Chipperfield, M.P.: Contribution of regional sources to atmospheric methane over the Amazon Basin in 2010 and 2011, *Global Biogeochem. Cycles*, *30(3)*, 400-420, doi:10.1002/2015GB005300, 2016.

5   Wunch, D., Toon, G.C., Blavier, J.F.L., Washenfelder, R.A., Notholt, J., Connor, B.J., Griffith, D.W., Sherlock, V. and Wennberg, P.O.: The total carbon column observing network, *Philos. Trans. Royal Soc. A.*, *369(1943)*, 2087-2112, doi:10.098/rsta.2010.0240, 2011
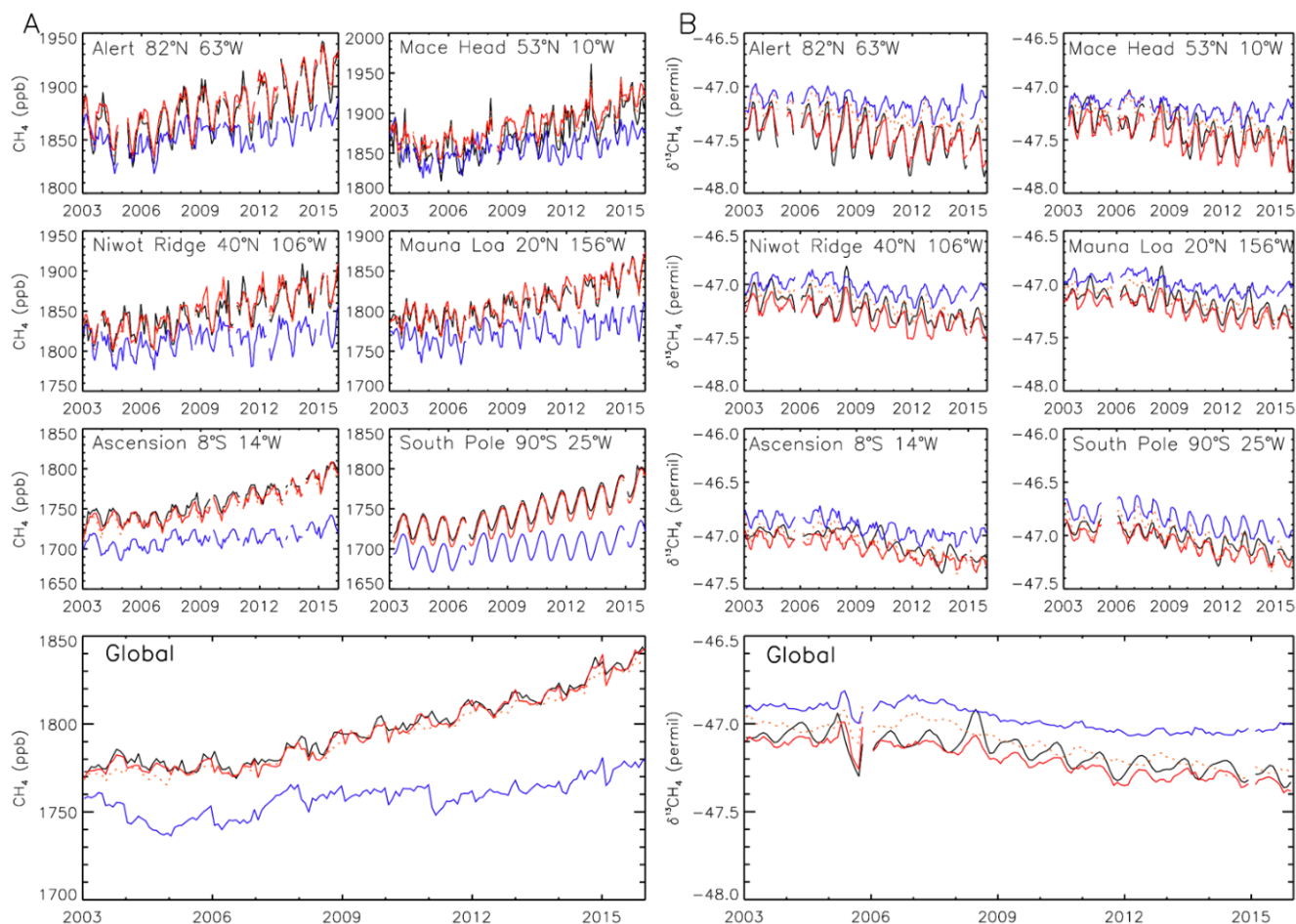
Figure 1. (a) Observed surface CH₄ (ppb, black solid line) from 2003 to 2015 at 6 selected NOAA sites and global mean. Also shown are results from TOMCAT simulations using prior emission estimates (blue solid), posterior estimates based on a CH₄ synthesis inversion (INV-CH4, red dotted) and posterior estimates based on a combined CH₄ and δ¹³CH₄ synthesis inversion (INV-FULL, red solid). (b) Same as (a) but for observed and modelled δ¹³CH₄. Global averages are based on site interpolations onto 180 1°-latitude bins, which are weighted by surface area.
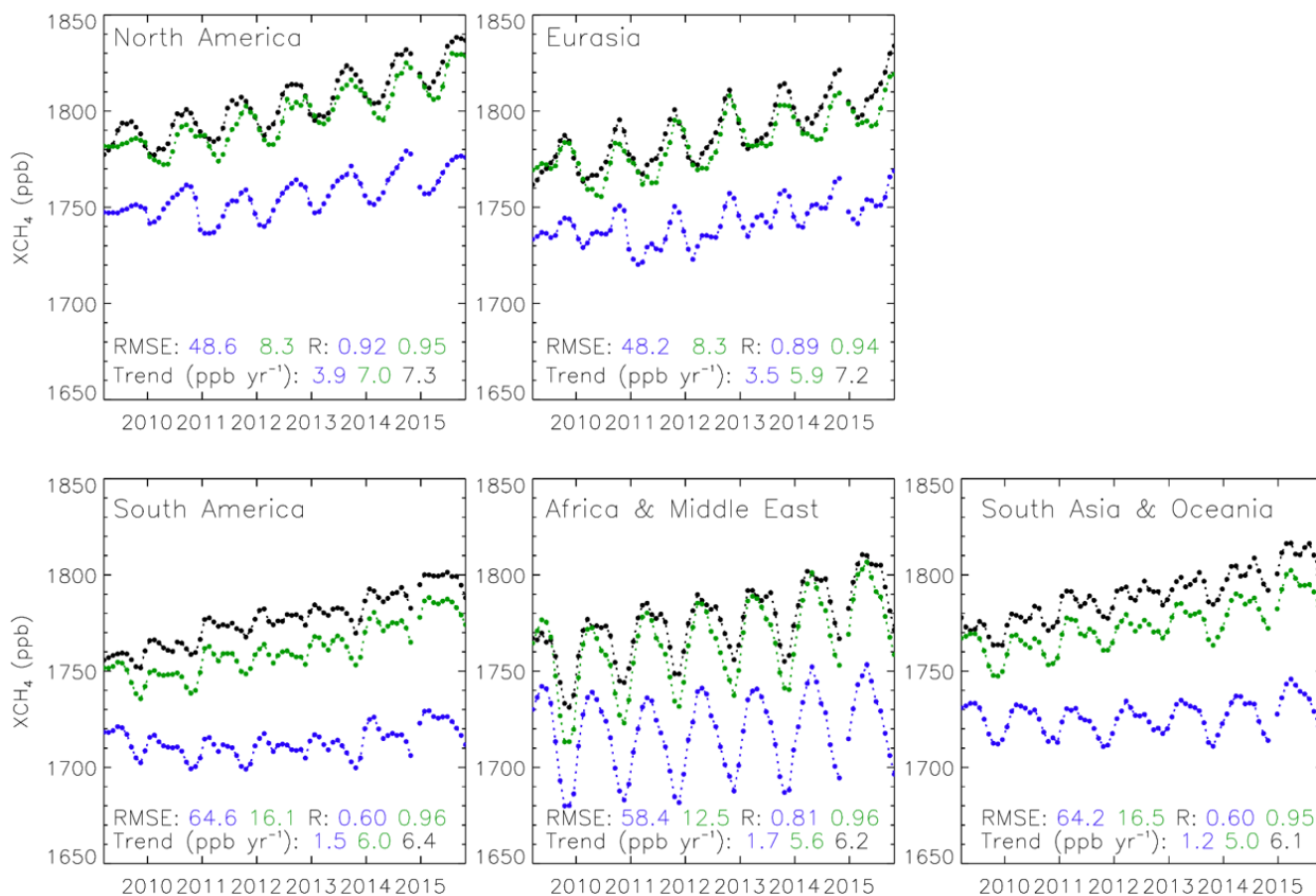
Figure 2. Monthly mean XCH₄ volume mixing ratio (ppb) from GOSAT between April 2009 and December 2015 (black line) for 5 emission regions. Also shown are results from TOMCAT simulations with prior (blue) and posterior (green) emission estimates, both with GOSAT averaging kernels applied. Correlation coefficients, RMSE and growth rates of the model simulations and GOSAT in each region are shown in the panels.
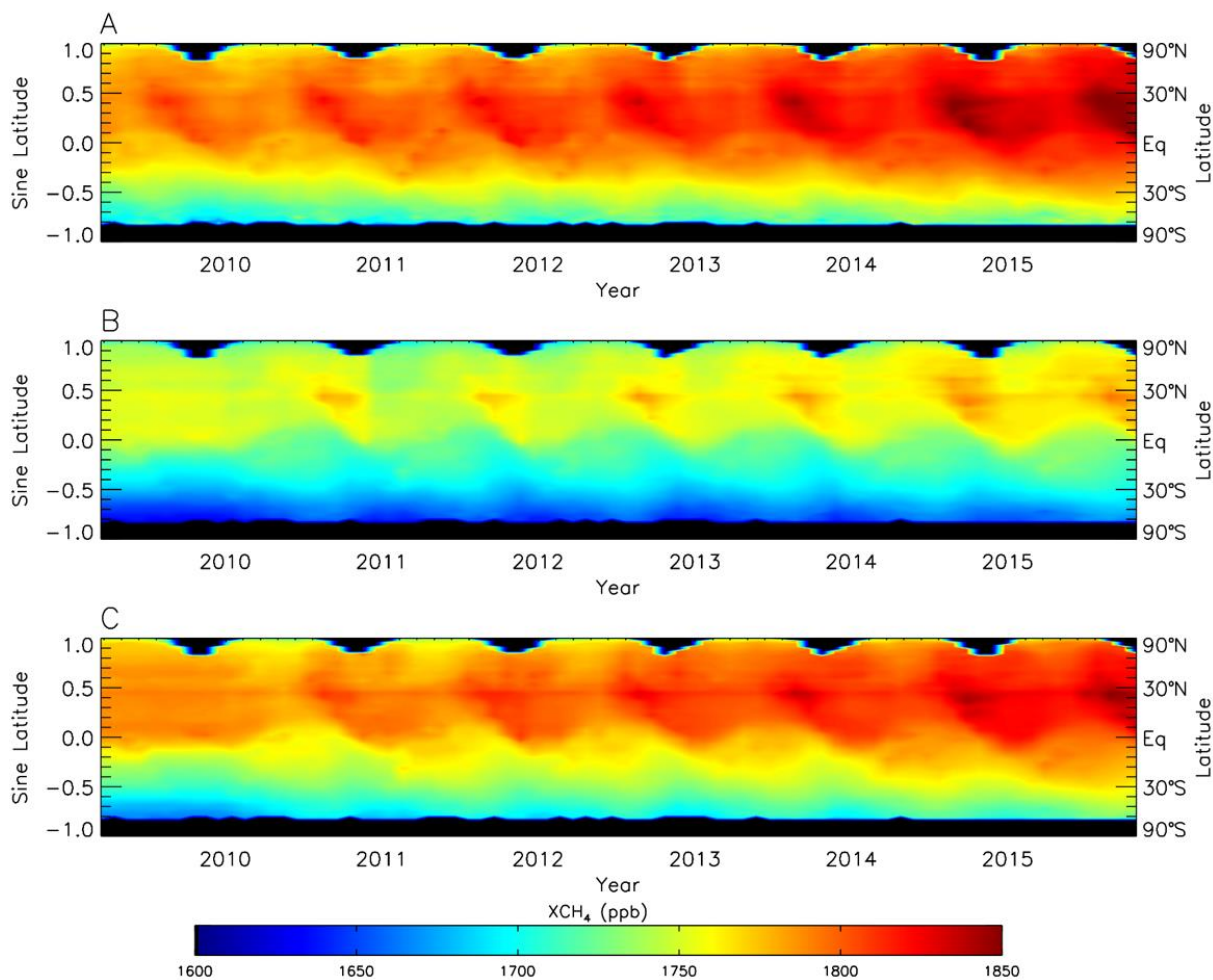
Figure 3. (a) Zonally averaged monthly mean XCH$_4$ volume mixing ratio (ppb) from GOSAT between April 2009 and December 2015 plotted against the sine of latitude, where black denotes missing values. (b and c) Same as (a) but for TOMCAT simulations with prior and posterior emission estimates, respectively. GOSAT averaging kernels are applied to model simulations.
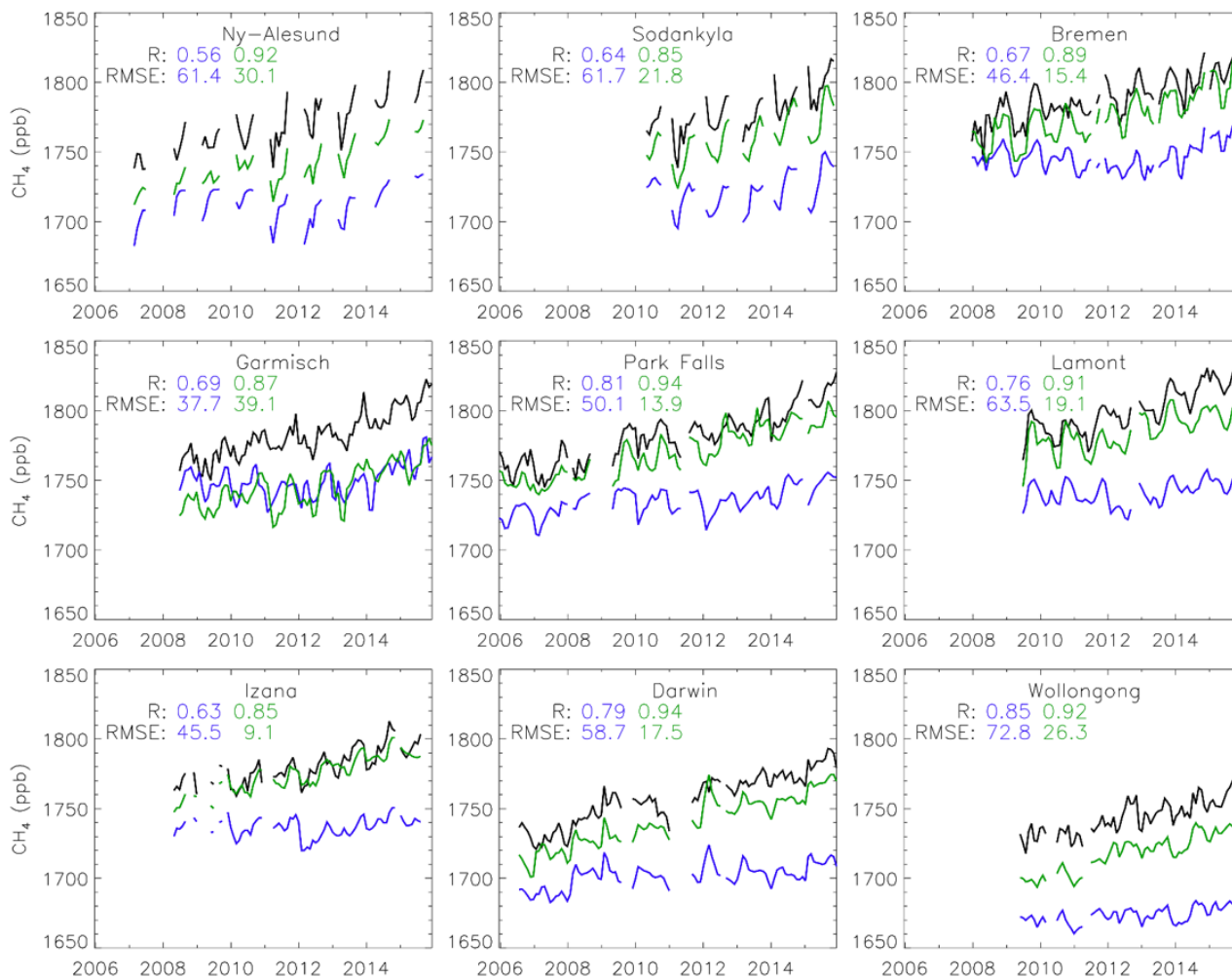
Figure 4. Observed monthly mean XCH4 volume mixing ratio (ppb) (blackline) at 9 TCCON sites. Also shown are results from TOMCAT simulations with prior (blue) and posterior (green) emission estimates, both with TCCON averaging kernels applied. Correlation coefficients and RMSE of the model simulations compared with TCCON are shown for each site.
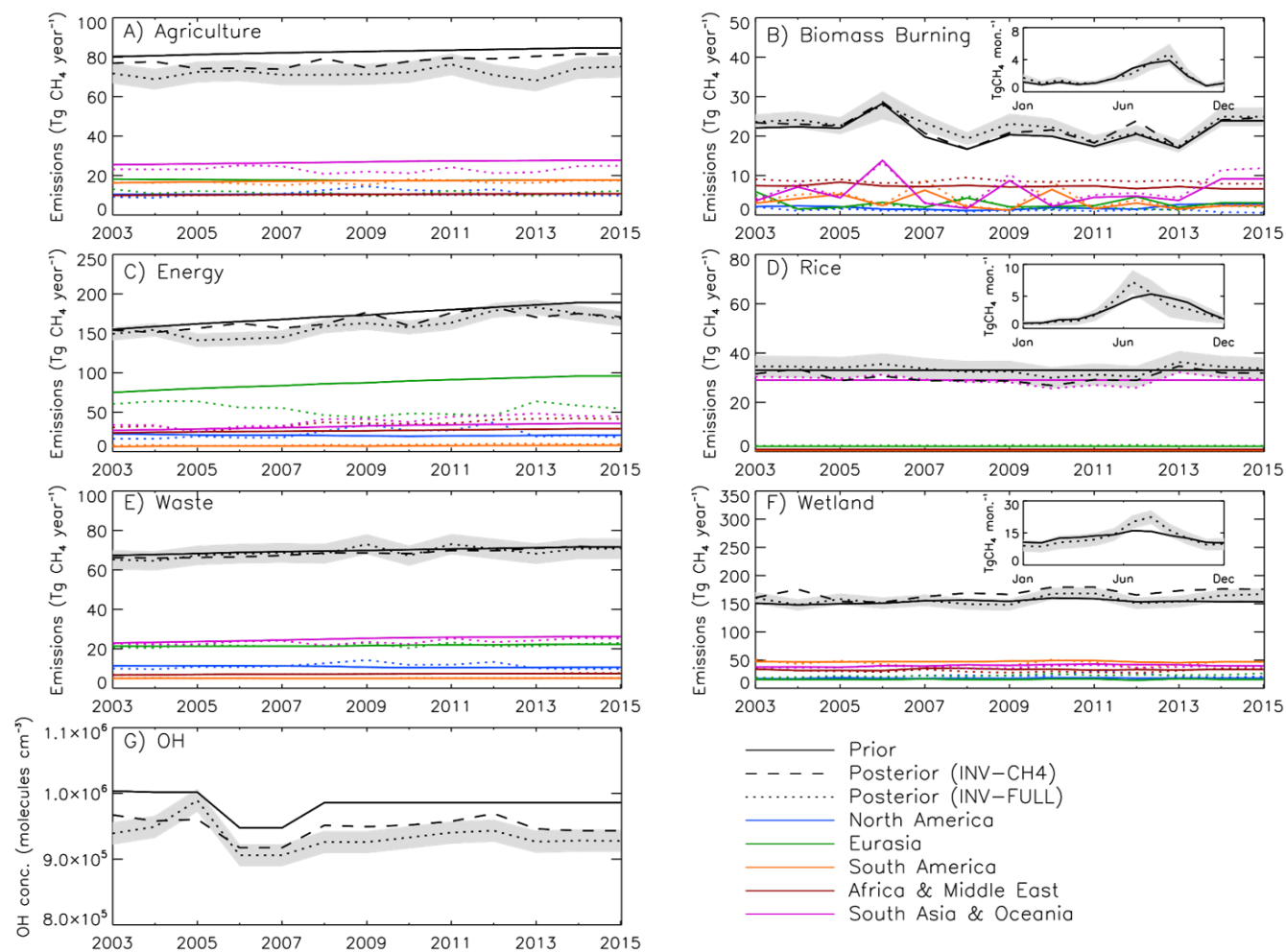
Figure 5. (a-f) Annual CH$_4$ emissions (Tg CH$_4$ year^{-1}) from different sectors for global prior (black solid line), INV-CH4 (black dashed line) and INV-FULL posterior (black dotted line) estimates. Regional estimates are also displayed for North America (blue), Eurasia (green), South America (orange), Africa and Middle East (red) and South Asia and Oceania (purple). (g) Prior and posterior global OH estimates for the same period. Shaded region denotes posterior error *A* for INV-FULL (see Eq. (5) in text).
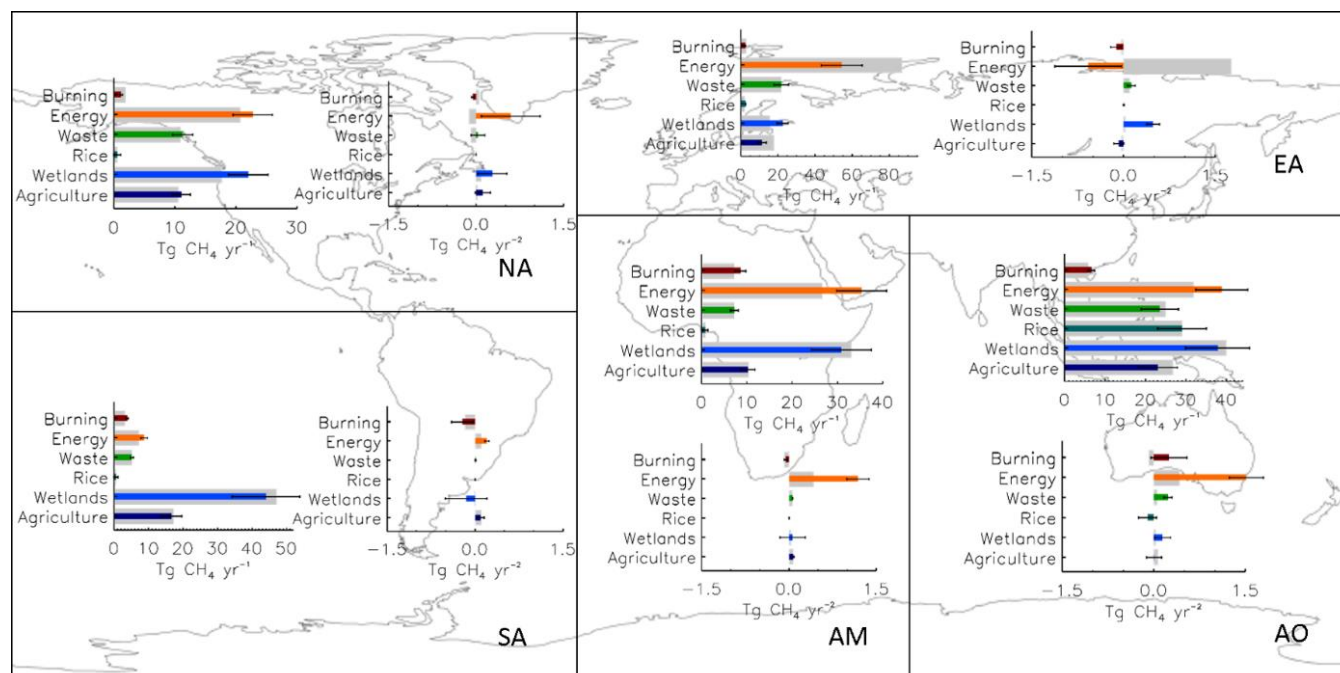
Figure 6. Map showing regional annual mean CH$_4$ emissions (Tg CH$_4$ year^{-1}) and yearly change in emissions (Tg CH$_4$ year^{-2}) calculated as a linear regression between 2003 and 2015 for INV-FULL (thin coloured bars) and prior (thick grey bars) estimates. Error bars represent one standard deviation of the mean posterior emissions and posterior regression errors. Note that the black borders indicate the 5 regions used for the flux partitioning.
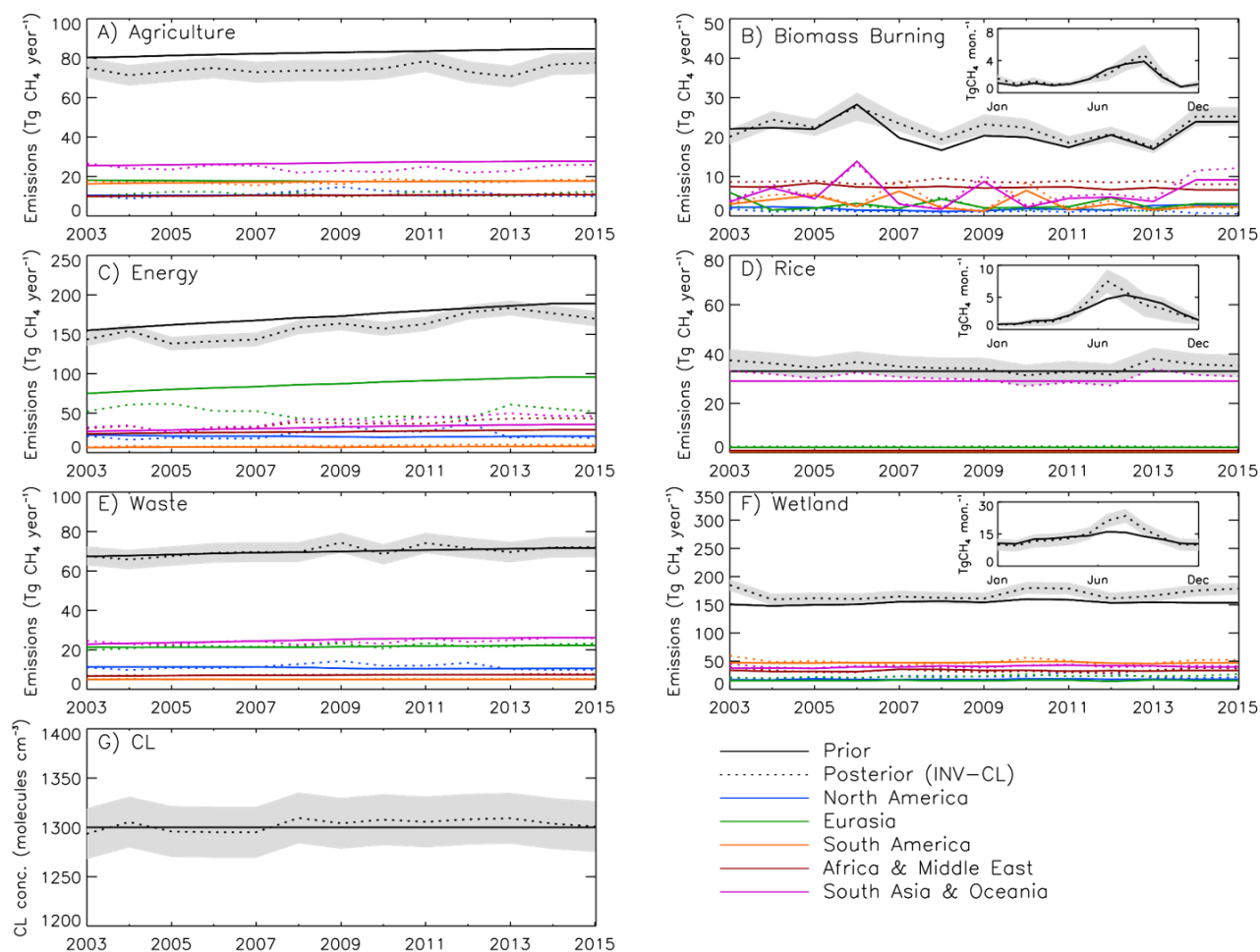
Figure 7. (a-f) Annual CH₄ emissions (Tg CH₄ year⁻¹) from different sectors for global prior (black solid line) and INV-CL (black dotted line) estimates. Regional estimates are also displayed for North America (blue), Eurasia (green), South America (orange), Africa and Middle East (red) and South Asia and Oceania (purple). (g) Prior and posterior global tropospheric Cl estimates for the same period. Shaded region denotes posterior error A (see Eq. (5) in text).
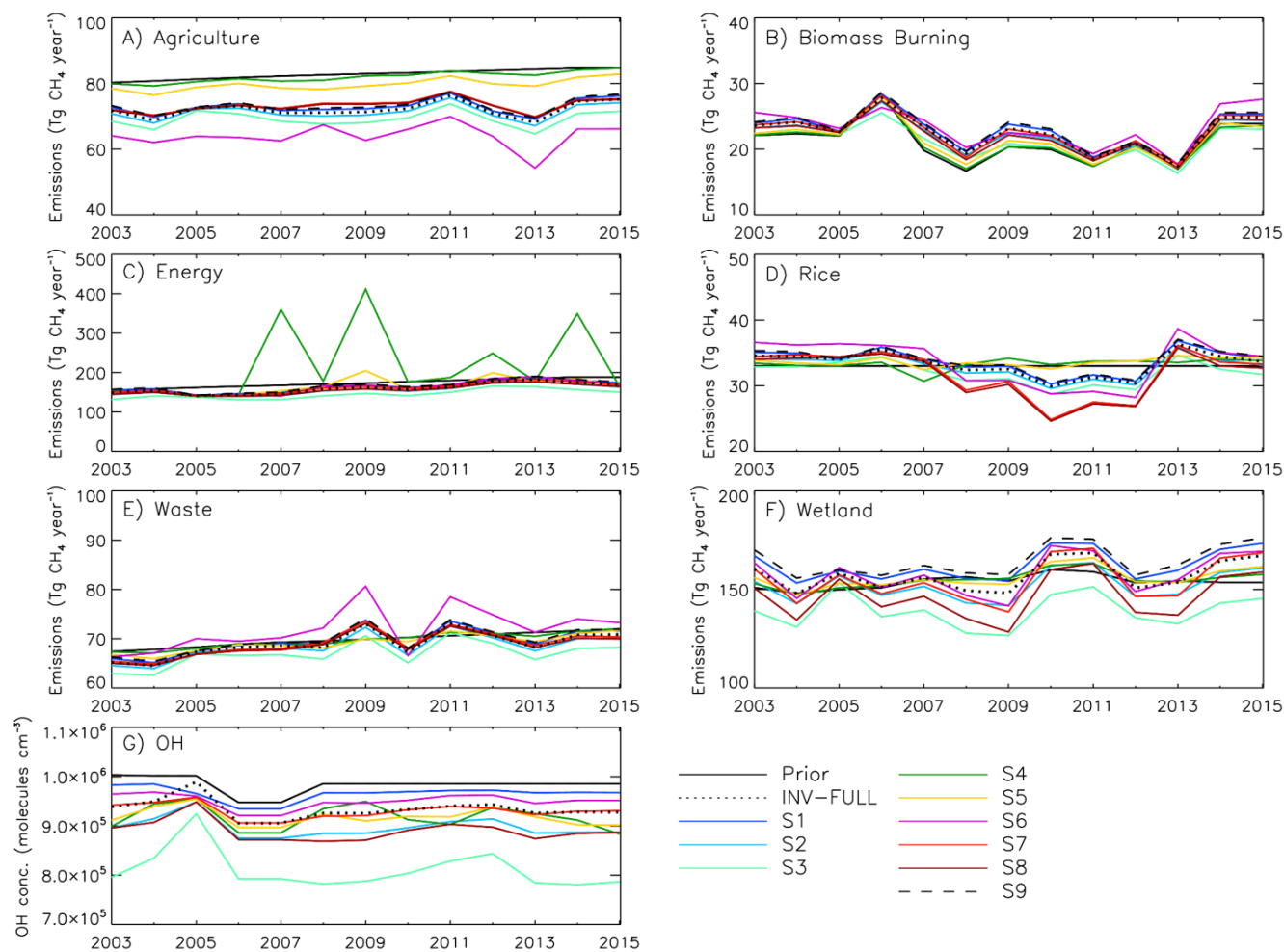
Figure 8. (a-f) Annual mean CH$_4$ emissions (Tg CH$_4$ year^{-1}) from different sectors for global prior (black solid line) and INV-FULL (black dotted line) estimates. (g) Same as (a-f) but for global mean OH (molecules cm^{-3}). Additional lines in each panel show sensitivity inversions with different emission and OH uncertainties (coloured lines), and an inversion assuming no change in OH (black dashed line).
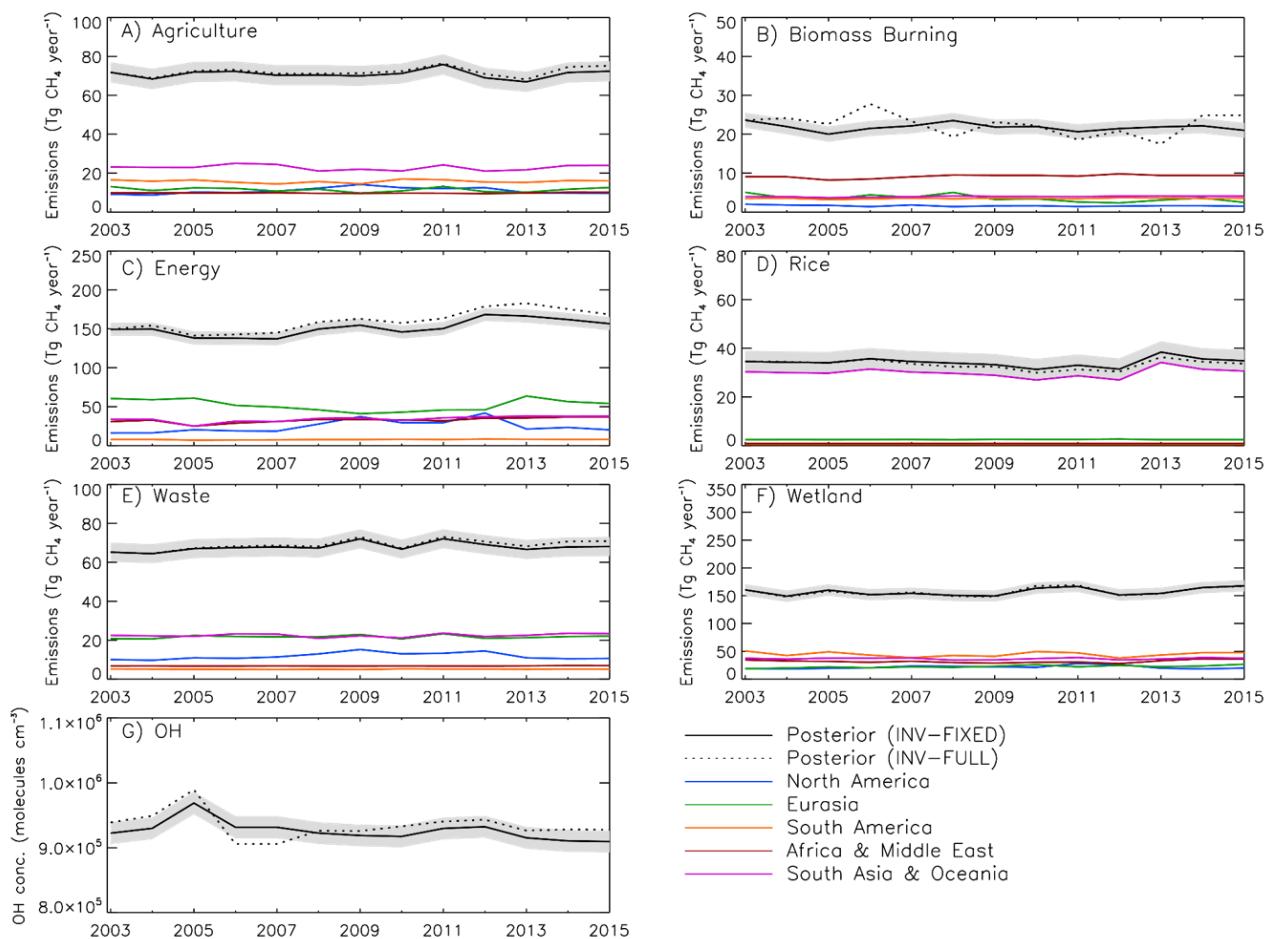
Figure 9. (a-f) Annual CH$_4$ emissions (Tg CH$_4$ year^{-1}) from different sectors for INV-FIXED (black solid line) and INV-FULL posterior (black dotted line) estimates. Regional estimates are also displayed for North America (blue), Eurasia (green), South America (orange), Africa and Middle East (red) and South Asia and Oceania (purple). (g) Prior and posterior global OH estimates (molecules cm^{-3}) for the same period. Shaded region denotes posterior error A (see Eq. (5) in text).

Source	$\delta^{13}CH_4$ (‰)	Emissions for 2003-2015 (Tg CH$_4$ yr^{-1})	
		Prior	Posterior
Agriculture (excluding rice)	-61.3	82.8	72.1
Biomass Burning	-22.2	21.1	22.5
Energy	-42.6	173.5	160.1
Rice	-62.0	33.0	33.3
Waste	-55.6	69.8	68.9
Wetlands	-61.0	153.8	157.2
Soil Methantrophy (negative emission)	22.0	-	-
Sink	Kinetic isotope effect ($^{12}CH_4/^{13}CH_4$)	Average concentration for 2003-2015 (molecules cm^{-3})	
		Prior	Posterior
OH	1.0039	0.98×10^6	0.93×10^6
Cl	1.06	1.3×10^3	1.3×10^3
O(^{1}D)	1.013	-	-

Table 1. Source and sink isotope signatures used in the TOMCAT 3-D CTM. Values for prior emissions (Kirschke *et al.*, 2013 McNorton *et al.*, 2016a, Schwietzke *et al.*, 2016) and isotope signatures (Saueressig *et al.*, 2001; Mikaloff-Fletcher *et al.*, 2004; Feilberg *et al.*, 2005; Whiticar *et al.*, 2007; Schwietzke *et al.*, 2016) are based on previous studies. Note that the soil sink is modelled as a negative emission.

Site Code	Site Name	Latitude (°N)	Longitude (°E)	Altitude (m)	Measurements
ALT	Alert, Canada	82.5	-62.5	190.0	CH_4, $\delta^{13}CH_4$
ASC	Ascension Island, UK	-8.0	-14.4	85.0	CH_4, $\delta^{13}CH_4$
AZR	Terceira Island, Portugal	38.8	-27.4	19.0	CH_4, $\delta^{13}CH_4$
BRW	Barrow, USA	71.3	-156.6	11.0	CH_4, $\delta^{13}CH_4$
CBA	Cold Bay, USA	55.2	-162.7	21.3	CH_4
HBA	Halley Station, UK	-75.6	-26.2	30.0	CH_4
ICE	Storhofdi, Iceland	63.4	-20.3	118.0	CH_4
KUM	Cape Kumukahi, USA	19.5	-154.8	3.0	CH_4, $\delta^{13}CH_4$
MHD	Mace Head, Ireland	53.3	-9.9	5.0	CH_4, $\delta^{13}CH_4$
MLO	Mauna Loa, USA	19.5	-155.6	3397.0	CH_4, $\delta^{13}CH_4$
NWR	Niwot Ridge, USA	40.1	-105.6	3523.0	CH_4, $\delta^{13}CH_4$
PAL	Pallas-Sammaltunturi, Finland	68.0	24.1	565.0	CH_4
PSA	Palmer Station, USA	-64.9	-64.0	10.0	CH_4
RPB	Ragged Point, Barbados	13.2	-59.4	15.0	CH_4
SMO	Tutuila, American Samoa	-14.2	-170.6	42.0	CH_4, $\delta^{13}CH_4$
SPO	South Pole, USA	-90.0	-24.8	2810.0	CH_4, $\delta^{13}CH_4$
STM	Ocean Station M, Norway	66.0	2.0	0.0	CH_4
SUM	Summit, Greenland	72.6	-38.4	3209.5	CH_4
THD	Trinidad Head, USA	41.1	-124.2	107.0	CH_4
WLG	Mt. Waliguan, China	36.3	100.9	3810.0	CH_4, $\delta^{13}CH_4$
ZEP	Ny-Alesund, Norway/Sweden	78.9	11.9	474.0	CH_4

Table 2. NOAA measurements from 2003 to 2015 used in the synthesis inversions of CH_4 (Dlugokencky *et al.*, 2017) and $\delta^{13}CH_4$ (White *et al.*, 2017).

Site Name	Latitude (∘N)	Longitude (∘E)	Altitude (km)	Reference
Ny-Alesund, Norway	78.9	11.9	0.02	Notholt *et al*. 2017a
Sodankyla, Finland	67.4	26.6	0.19	Kivi *et al*. 2017
Bremen, Germany	53.1	8.9	0.03	Notholt *et al*. 2017b
Garmisch, Germany	47.5	11.1	0.74	Sussmann *et al*. 2017
Park Falls, USA	45.9	-90.3	0.44	Wennberg *et al*. 2017a
Lamont, USA	36.6	-97.5	0.32	Wennberg *et al*. 2017b
Izana, Spain	28.3	-16.5	2.37	Blumenstock *et al*. 2017
Darwin, Australia	-12.5	130.9	0.04	Griffith *et al*. 2017a
Wollongong, Australia	-34.4	150.9	0.03	Griffith *et al*. 2017b

Table 3. TCCON sites (Wunch *et al*. 2011) used for evaluation of the TOMCAT simulations.

Region	Annual Emissions by Sector (Tg CH$_4$ year^{-1})						
	Biomass Burning	Energy	Waste	Rice	Wetlands	Agriculture	Total
North America	1.2	22.8	11.2	0.5	22.0	11.0	68.7
Eurasia	2.3	54.4	21.7	2.5	22.5	11.2	114.6
South America	3.8	8.7	5.1	0.5	44.0	16.6	78.7
Africa & Middle East	8.6	35.4	7.2	0.8	30.8	10.2	93.1
South Asian & Oceania	6.6	38.9	23.6	29.0	37.9	23.1	159.1
Global	22.5	160.1	68.9	33.3	157.2	72.1	537.5

Table 4. Regional CH$_4$ emissions based on synthesis inversion estimates between 2003 and 2015. Note the total global emission, but not the total regional emissions, include the supplementary emissions (geological, hydrates, oceans and termites).

Region	Annual Emission Growth by Sector (Tg CH_4 year^{-2})						
	Biomass Burning	Energy	Waste	Rice	Wetlands	Agriculture	Total
North America	-0.06	+0.59	+0.03	+0.00	+0.28	+0.11	+0.95
Eurasia	-0.12	-0.58	+0.13	+0.00	+0.48	-0.08	-0.17
South America	-0.22	+0.20	+0.01	+0.00	-0.15	+0.09	-0.06
Africa & Middle East	-0.05	+1.18	+0.06	+0.00	+0.06	+0.07	+1.33
South Asian & Oceania	+0.25	+1.51	+0.23	-0.10	+0.14	+0.00	+2.03
Global	-0.20	+2.91	+0.46	-0.10	+0.81	+0.20	+4.08

Table 5. Regional CH_4 emission growth trends based on synthesis inversion estimates between 2003 and 2015.

Simulation	Annual Emission by Sector for the 2003-2006 Period (Tg CH$_4$ year^{-1})						
	Biomass Burning	Energy	Waste	Rice	Wetlands	Agriculture	Total
INV_FULL	24.5	146.9	66.3	34.6	154.4	71.6	518.9
INV_CH4	24.4	156.0	66.3	31.1	160.7	75.9	529.8
INV_FIXED	21.8	143.8	66.1	34.6	155.4	71.1	514.6
	Annual Emission by Sector for the 2007-2015 Period (Tg CH$_4$ year^{-1})						
	Biomass Burning	Energy	Waste	Rice	Wetlands	Agriculture	Total
INV_FULL	21.6	165.9	70.1	32.7	158.4	72.3	545.8
INV_CH4	20.9	169.9	69.6	30.0	171.9	78.7	557.7
INV_FIXED	21.8	154.5	68.7	34.0	158.1	70.9	536.1
	Difference in Annual Emission Between 2007-2015 and 2003-2006 (Tg CH$_4$ year^{-1})						
	Biomass Burning	Energy	Waste	Rice	Wetlands	Agriculture	Total
INV_FULL	-2.9	+19.0	+3.8	-1.9	+4.0	+0.7	+26.9
INV_CH4	-3.5	+13.9	+3.3	-1.1	+11.2	+2.8	+27.9
INV_FIXED	0.0	+10.7	+2.6	-0.6	+2.7	-0.2	+21.5

Table 6. Posterior annual CH$_4$ emission for the period of near-zero atmospheric growth (2003-2006) and the renewed growth (2007-2015) based on three different inversion simulations. Note the total emissions, include the supplementary emissions (geological, hydrates, oceans and termites).

Source/sink	Sensitivity Test Error									
	Control	S1	S2	S3	S4	S5	S6	S7	S8	S9
Wetlands	50%	50%	50%	50%	10%	20%	100%	100%	100%	50%
Rice	50%	50%	50%	50%	10%	20%	100%	100%	100%	50%
Agriculture (excluding rice)	50%	50%	50%	50%	10%	20%	100%	50%	50%	50%
Waste	50%	50%	50%	50%	10%	20%	100%	50%	50%	50%
Energy	50%	50%	50%	50%	10%	20%	100%	50%	50%	50%
Biomass Burning	50%	50%	50%	50%	10%	20%	100%	50%	50%	50%
OH	2%	1%	3%	10%	2%	2%	2%	2%	3%	0%

Table 7. Suite of inversion sensitivity experiments with varying errors on source and sink estimates.